

Quasi-linear gyrokinetic predictions of the Coriolis momentum pinch in National Spherical Torus Experiment

W. Guttenfelder, S. M. Kaye, Y. Ren, W. Solomon, R. E. Bell, J. Candy, S. P. Gerhardt, B. P. LeBlanc, and H. Yuh

Citation: *Physics of Plasmas* **23**, 052508 (2016); doi: 10.1063/1.4948791

View online: <http://dx.doi.org/10.1063/1.4948791>

View Table of Contents: <http://scitation.aip.org/content/aip/journal/pop/23/5?ver=pdfcov>

Published by the [AIP Publishing](#)

Articles you may be interested in

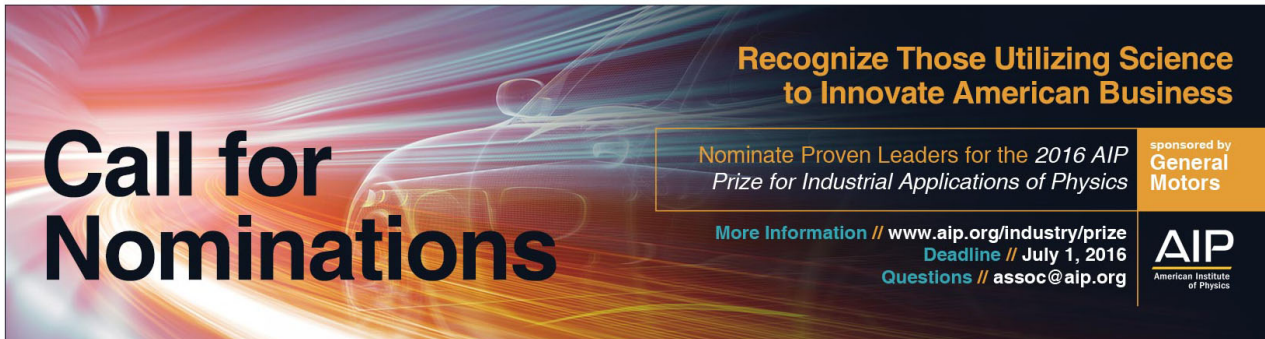
[Influence of centrifugal effects on particle and momentum transport in National Spherical Torus Experiment](#)
Phys. Plasmas **22**, 082307 (2015); 10.1063/1.4928427

[Reduced model prediction of electron temperature profiles in microtearing-dominated National Spherical Torus eXperiment plasmas](#)
Phys. Plasmas **21**, 082510 (2014); 10.1063/1.4893135

[Characterization and parametric dependencies of low wavenumber pedestal turbulence in the National Spherical Torus Experimenta\)](#)
Phys. Plasmas **20**, 055903 (2013); 10.1063/1.4803913

[Scaling of linear microtearing stability for a high collisionality National Spherical Torus Experiment discharge](#)
Phys. Plasmas **19**, 022506 (2012); 10.1063/1.3685698

[Nonlinear gyrokinetic theory of toroidal momentum pinch](#)
Phys. Plasmas **14**, 072302 (2007); 10.1063/1.2743642



Call for Nominations

Recognize Those Utilizing Science to Innovate American Business

Nominate Proven Leaders for the 2016 AIP Prize for Industrial Applications of Physics

More Information // www.aip.org/industry/prize
Deadline // July 1, 2016
Questions // assoc@aip.org

sponsored by General Motors

AIP
American Institute of Physics

Quasi-linear gyrokinetic predictions of the Coriolis momentum pinch in National Spherical Torus Experiment

W. Guttenfelder,^{1,a)} S. M. Kaye,¹ Y. Ren,¹ W. Solomon,¹ R. E. Bell,¹ J. Candy,²
 S. P. Gerhardt,¹ B. P. LeBlanc,¹ and H. Yuh³

¹Princeton Plasma Physics Laboratory, Princeton, New Jersey 08543, USA

²General Atomics, San Diego, California 92186, USA

³Nova Photonics Inc., Princeton, New Jersey 08540, USA

(Received 7 March 2016; accepted 31 March 2016; published online 11 May 2016)

This paper presents quasi-linear gyrokinetic predictions of the Coriolis momentum pinch for low aspect-ratio National Spherical Torus Experiment (NSTX) H-modes where previous experimental measurements were focused. Local, linear calculations predict that in the region of interest (just outside the mid-radius) of these relatively high-beta plasmas, profiles are most unstable to microtearing modes that are only effective in transporting electron energy. However, sub-dominant electromagnetic and electrostatic ballooning modes are also unstable, which are effective at transporting energy, particles, and momentum. The quasi-linear prediction of transport from these weaker ballooning modes, assuming they contribute transport in addition to that from microtearing modes in a nonlinear turbulent state, leads to a very small or outward convection of momentum, inconsistent with the experimentally measured inward pinch, and opposite to predictions in conventional aspect ratio tokamaks. Additional predictions of a low beta L-mode plasma, unstable to more traditional electrostatic ion temperature gradient-trapped electron mode instability, show that the Coriolis pinch is inward but remains relatively weak and insensitive to many parameter variations. The weak or outward pinch predicted in NSTX plasmas appears to be at least partially correlated to changes in the parallel mode structure that occur at a finite beta and low aspect ratio, as discussed in previous theories. The only conditions identified where a stronger inward pinch is predicted occur either in the purely electrostatic limit or if the aspect ratio is increased. As the Coriolis pinch cannot explain the measured momentum pinch, additional theoretical momentum transport mechanisms are discussed that may be potentially important. *Published by AIP Publishing.*

[<http://dx.doi.org/10.1063/1.4948791>]

I. INTRODUCTION

Understanding the transport of toroidal angular momentum in tokamaks is important as rotation and rotation shear can influence many processes such as resistive wall modes (RWMs)^{1–4} and micro-turbulence.^{5–8} Furthermore, simultaneously investigating transport in multiple channels, like momentum, impurity/particle and heat, can provide a stronger constraint on theoretical predictions as opposed to investigating a single transport channel with no consideration for a complete consistent solution.^{9,10} While a diffusive momentum transport contribution has long been theoretically predicted¹¹ and measured,¹² more recently a convective contribution has also been predicted and measured using perturbative approaches.¹³ Understanding this additional contribution is important as future devices like ITER will have relatively small injected torque, and the rotation profile will depend strongly on both convective momentum transport and any intrinsic sources of torque.¹⁴

The transport of toroidal angular momentum $L = nm\langle R^2 \rangle \Omega$ (where n is the ion density, m is the ion mass, R is major radius, $\langle \dots \rangle$ represents the flux surface average, and Ω is the toroidal angular rotation) is often considered to be composed of three general parts

$$\Pi = nm\langle R^2 \rangle [-\chi_\phi \nabla \Omega + (V_\phi + \Gamma_n/n)\Omega] + \Pi_{RS} \quad (1)$$

including diffusion (χ_ϕ) proportional to rotation gradient, convection (including a momentum specific convection V_ϕ and regular particle convection Γ_n) proportional to rotation itself, and any other “residual stress” contributions (Π_{RS}) not explicitly dependent on rotation or rotation gradient (which can also be thought of as the source of intrinsic torque). The diffusive component is typically characterized by the Prandtl number $Pr = \chi_\phi / \chi_{i,i}$, the ratio of momentum to ion thermal diffusivity, which is order unity as expected from turbulence theory.¹¹ Ignoring the residual stress term, multiple tokamak experiments, using perturbative methods, have inferred the presence of a momentum pinch,¹⁵ with a normalized pinch parameter RV_ϕ / χ_ϕ ranging between -1 and -10 . Furthermore, in dedicated JET scans,¹⁶ the predicted pinch was found to depend on density gradient, with a weaker dependence on safety factor and independence on collisionality. These trends were reproduced by performing statistical analysis over a large database of JET discharges,^{17,18} where dependencies of momentum pinch on magnetic shear and minor radius (r/R , as an indicator for trapped particle fraction) were also identified.

The strength of the measured pinch and most of the parametric dependencies have been predicted by local, quasi-linear gyrokinetic theory that is based on the Coriolis pinch^{19–25} (which can equivalently be considered as a combination of

^{a)}E-mail: wgutten@pppl.gov

turbulent equipartition (TEP), and thermoelectric effects; see Refs. 21 and 23). Specifically, for a conventional aspect ratio ($R/a \sim 3$), the quasi-linear prediction of momentum pinch from electrostatic ion temperature gradient (ITG) instabilities predicts dependences on density gradient, safety factor, and minor radius (i.e., particle trapping) that reproduces many of the measurements and trends.^{17,18,26}

A strong inward momentum pinch has also been observed in low-aspect-ratio ($R/a \sim 1.5$) H-mode discharges in the National Spherical Torus Experiment (NSTX).^{27–29} The corresponding pinch parameter RV_ϕ/χ_ϕ is similar in value to that observed in conventional aspect ratio, and the measured pinch appears to be somewhat consistent with the analytic theory predictions that were based on ITG turbulence in low-beta conventional aspect ratio.²⁸ However, the NSTX H-modes are at substantially higher beta and lower-aspect ratio, and previous gyrokinetic analysis in other similar NSTX H-modes suggests that the traditional electrostatic ITG or trapped electron mode (TEM) instabilities are often not expected in the core confining region ($r/a \sim 0.5–0.8$). Instead, fundamentally electromagnetic instabilities such as microtearing modes (MTMs) and kinetic ballooning modes (KBMs) are often predicted.³⁰ Microtearing modes only predict significant electron heat fluxes,^{31–34} and so KBMs should be investigated as a potential source of momentum pinch. Previous theory work for conventional aspect ratio³⁵ showed that as beta is increased for ITG modes, Prandtl and pinch numbers become smaller, and the pinch can even reverse direction as the mode transitions to KBM, leading to an outward convection, although no significant correlation of RV_ϕ/χ_ϕ with beta was found in the statistical database approach of JET H-mode data.^{17,18}

Given the success of local, quasi-linear gyrokinetic theory in describing momentum pinches in conventional aspect ratio tokamaks, and the encouraging initial agreement found between NSTX H-mode experiments and analytic theory estimates, in this paper we present the equivalent local, quasi-linear predictions of Pr and RV_ϕ/χ_ϕ directly for the perturbative momentum experiments conducted in NSTX.^{27,28} This work stems from a joint International Tokamak Physics Activity (ITPA) effort to compare momentum transport and its parametric dependencies across different tokamaks²⁶ to support predictions for ITER and next-generation devices. There are additional complications that

arise when interpreting the momentum transport analysis in NSTX. Most significantly, the ion thermal transport in NSTX H-modes is typically near neoclassical predictions,^{36–38} so the concept of a purely turbulent Prandtl number ($\chi_{\phi,\text{turb}}/\chi_{i,\text{turb}}$) is often ill-defined as $\chi_{i,\text{exp}} \approx \chi_{i,\text{NC}} > \chi_{i,\text{turb}}$. On the other hand, since the neoclassical contribution to the momentum transport appears to be negligible ($\Pi_{\text{turb}} \gg \Pi_{\text{NC}}$),²⁸ the normalized pinch parameter is assumed to be a ratio of pure turbulence quantities ($RV_{\phi,\text{turb}}/\chi_{\phi,\text{turb}}$) and it is therefore more suitable to compare this dimensionless quantity with predictions from micro-stability theory.

The remainder of this paper is organized as follows. Section II discusses the experimental discharges under investigation as well as the details relevant for the simulations. Section III then shows example linear stability and quasi-linear predictions of momentum pinch. As will be shown, local gyrokinetic theory does not appear to describe the measured inward momentum pinch in these NSTX high-beta H-mode experiments. This is partially attributed to the presence of electromagnetic instabilities at high beta, as well as characteristics of the parallel mode structure on the Coriolis pinch. In an attempt to connect with conventional aspect ratio tokamak results, Section IV presents quasi-linear results for a lower beta NSTX L-mode plasma unstable to traditional electrostatic ITG-TEM drift waves. Even for these cases at low beta, the predicted pinch is relatively weak. Parametric dependences of the theoretical pinch are shown, illustrating the important role of trapped particle fraction and aspect ratio. We summarize the results in Sec. V, where we also discuss additional physical mechanisms that may be responsible for the observed inward momentum pinch which are presently being investigated.

II. EXPERIMENTAL AND NUMERICAL PARAMETERS

The discharges under investigation are NSTX H-modes with toroidal magnetic fields between $B_T = 0.35–0.55$ T, plasma currents $I_p = 0.7–1.1$ MA, line-averaged densities $\langle n_e \rangle = 4.8–7.3 \times 10^{19} \text{ m}^{-3}$, and neutral beam injection (NBI) heating powers $P_{\text{NBI}} = 3.9–5.8$ MW. Short (50 ms) $n = 3$ nonresonant magnetic perturbations (nRMP) were applied to briefly perturb the plasma rotation, and the response after this perturbation was used to infer χ_ϕ and V_ϕ (assuming there is no contribution from residual stress).^{27,28} The following gyrokinetic simulations used profiles and equilibrium reconstruction data at a time during this analysis period given in

TABLE I. Relevant discharge parameters for the seven H-modes (H1–H7) and an L-mode (L1) under investigation, including shot number, time of interest (t), nominal toroidal magnetic field (B_T), plasma current (I_p), NBI heating power (P_{NBI}), line-averaged density (n_e), edge safety factor (q_{95}), toroidal beta (β_T), normalized beta (β_N), and electron collisionality (ν_{*e}) and $1/\rho_*$, both evaluated at $\rho = 0.65$.

Case	Shot	t (s)	B_T (T)	I_p (MA)	P_{NBI} (MW)	$\langle n_e \rangle$ (10^{19} m^{-3})	q_{95}	β_T (%)	β_N	$\nu_{*e} (\rho = 0.65)$	$1/\rho_* (\rho = 0.65)$
H1	134 751	0.485	0.45	0.9	3.9	5.8	9.3	11.9	3.5	0.24	95
H2	134 778	0.735	0.45	0.9	3.9	7.3	8.6	14.2	4.2	0.57	89
H3	134 779	0.435	0.45	0.9	3.9	5.1	9.2	11.8	3.5	0.24	89
H4	134 780	0.435	0.45	0.9	3.9	5.2	9.2	12.2	3.7	0.30	92
H5	134 780	0.735	0.45	0.9	3.9	7.2	8.4	15.2	4.6	0.61	88
H6	134 783	0.485	0.55	1.1	5.8	6.0	9.3	13.8	4.0	0.089	88
H7	134 790	0.435	0.35	0.7	3.8	4.8	9.0	15.6	4.6	0.31	77
L1	141 716	0.448	0.55	0.9	1.9	2.6	9.7	7.0	2.8	0.096	176

Table I. Also shown are additional equilibrium parameters of interest, including edge safety factor $q_{95} = 8.4\text{--}9.3$, toroidal beta $\beta_T = 11.8\%\text{--}15.6\%$, normalized beta $\beta_N = \beta_T \cdot a B_T / I_p = 3.5\text{--}4.6$, electron collisionality $\nu_{*e} = (\nu^{ei}/\epsilon)/(\epsilon^{1/2} \cdot v_{Te}/qR)$, and inverse normalized gyroradius, $1/\rho^* = a/\rho_i$, where $\rho_i = (T_i/m_D)^{1/2}/B_T$. Both ν_{*e} and ρ^* are evaluated at $\rho = 0.65$, where ρ is a normalized flux-surface coordinate defined using the square root of normalized toroidal flux.

The Eulerian gyrokinetic code GYRO^{39–41} was used to calculate linear stability and quasi-linear transport based on these discharges. The simulations include kinetic electrons, deuterium and carbon ions, shear magnetic perturbations ($\delta B_{\perp} = \nabla \times \delta A_{\parallel}$), compressional magnetic perturbations (δB_{\parallel}), and electron pitch angle scattering. When included in the simulations, flow effects are treated in the linear limit (i.e., no centrifugal effects are accounted for). Geometric quantities are derived from numerical equilibrium reconstructions using LRDFIT⁴² that are constrained by external magnetic signals, diamagnetic flux, internal magnetic pitch angle (via E_R corrected Motional Stark effect measurements⁴³), and an isotherm requirement [$T_e(R) \rightarrow T_e(\psi)$] using full profile Thomson scattering measurements.⁴⁴ Linear simulations typically use 16–32 radial grid points (to resolve resonant current perturbations of microtearing modes), 12–16 energy grid points, 12 pitch angles, and 14 parallel orbit mesh points ($\times 2$ signs of parallel velocity), as determined from convergence tests. The quasi-linear prediction of momentum fluxes from GYRO has been successfully benchmarked with other gyrokinetic codes.⁴⁵

The experimental analysis of momentum transport focused on the region of $\rho = 0.5\text{--}0.7$, which corresponds to the mid-plane half-diameter $r/a \approx 0.6\text{--}0.8$ used in GYRO. Table II lists the relevant local equilibrium and plasma parameters that determine linear stability in the middle of this region ($r/a = 0.7$) for the same shots in Table I, including local safety factor (q), magnetic shear ($s = -r/q \cdot dq/dr$), ratio of electron to ion temperature, and normalized temperature and density gradients ($a/L_X = -a/X \cdot dX/dr$). The local electron beta is defined as $\beta_e = 8\pi n_e T_e / B^2$ using the vacuum values of $B_T = [0.35\text{--}0.55]$ T listed in Table I. A second set of values $\beta_{e,\text{unit}}$ are defined replacing B_T with the quantity $B_{\text{unit}} = B_T \cdot \rho / r \cdot d\rho/dr$ [$\rho = (\Psi/\pi B_T)^{1/2}$, Ψ_t is the toroidal flux] as used in normalizations throughout GYRO. The parameter $\alpha_{\text{MHD}} = -q^2 R_0^2 8\pi / B_{\text{unit}}^2 \cdot dp/dr$ is a generalized MHD- α parameter.⁴⁶ The normalized electron-ion collision frequency

is determined by $\nu^{ei} = Z_{\text{eff}} \nu_{ei}$, where $\nu_{ei} = 4\pi n_e e^4 \log \Lambda / (2T_e)^{3/2} m_e^{1/2}$ depends only on n_e and T_e . The effective charge Z_{eff} is determined assuming only a carbon impurity (carbon density and rotation profiles are measured using CHERS⁴⁷). The Mach number, $Ma = u = R\Omega/c_s$, and toroidal rotation shear, $u' = -R^2 \delta\Omega/c_s$, are normalized using the sound speed $c_s = (T_e/m_D)^{1/2}$. Assuming that the toroidal flow dominates the diamagnetic or poloidal flow contributions to E_r (appropriate for the core of NSTX NBI plasmas), the $E \times B$ shearing rate is given by $\gamma_E = -r/q \cdot d\Omega/dr = (r/qR) \cdot u' \cdot (c_s/R)$.⁴¹ Other normalizing quantities are the minor radius, $a \approx 0.59$ m, and deuterium gyroradius evaluated at the local electron temperature using $B_{\text{unit}}, \rho_{s,D} = (m_D T_e)^{1/2} / B_{\text{unit}}$.

III. H-MODE RESULTS

A. Linear spectra examples

As an example of linear stability calculations (first run without any flow effects, $u' = u = \gamma_E = 0$), Fig. 1 shows the real frequencies and growth rates for two different discharges from Table I (H1, H2, respectively). A broad spectrum of MTM modes up to $k_{\theta} \rho_s \leq 1$ (lines with dots) is found to be unstable from $r/a = 0.6\text{--}0.8$ in the region where the perturbative momentum transport analysis was performed. The features predicted are similar to those found in previous NSTX H-mode calculations: tearing-parity eigenfunctions (not shown), real frequencies that are proportional to the electron diamagnetic drift frequency, $\omega_r \approx \omega_{*e} = (k_{\theta} \rho_s) \cdot (a/L_{ne} + a/L_{Te}) \cdot (c_s/a)$, the only substantial (quasilinear) flux is in the electron thermal transport channel, and additional scans show the mode to be driven unstable by electron temperature gradient and finite beta. MTMs are predicted to be the strongest instability in the same region for all seven H-mode discharges analyzed, although in the lowest collisionality discharge (H6) the MTM is weaker or absent at a few locations due to the change in profile shapes (as noted in the previous analysis^{30,48,49}).

At a few radii in all discharges, additional ballooning parity modes are predicted to be unstable at lower wavenumbers (diamonds), with relatively small (or negative) real frequencies. The strength of these modes varies for the different discharges as illustrated for the two cases in Fig. 1. The GYRO eigenvalue solver⁵⁰ was used to determine the extent of the unstable spectra at $r/a = 0.75$ and is shown by the dashed line, where the modes are found to be unstable up to $k_{\theta} \rho_s \leq 0.5$.

TABLE II. Local ($r/a = 0.7$) equilibrium and plasma parameters relevant for linear stability used in the linear GYRO simulations for the discharges listed in Table I.

Case	q	s	T_e/T_i	a/L_{Te}	a/L_{Ti}	a/L_{ne}	β_e (%)	$\beta_{e,\text{unit}}$ (%)	α_{MHD}	ν_{ei} (c_s/a)	Z_{eff}	u	u'	γ_E (c_s/a)	n_e (10^{19}m^{-3})	T_e (eV)
H1	3.1	1.8	0.96	2.8	2.8	0.6	4.9	0.81	0.76	1.63	2.2	0.18	1.5	0.15	5.9	420
H2	3.3	1.6	0.93	3.4	2.3	0.6	6.3	0.94	1.05	1.88	3.1	0.16	1.0	0.08	7.5	430
H3	4.0	1.4	1.01	2.6	2.8	0.1	5.0	0.67	0.82	1.10	2.4	0.18	1.8	0.13	5.3	480
H4	4.0	1.2	1.07	2.7	3.3	-0.2	5.2	0.67	0.86	1.13	2.5	0.16	1.8	0.12	5.5	480
H5	3.2	1.4	0.91	4.0	2.6	0.6	6.5	0.97	1.07	1.83	3.2	0.18	1.1	0.09	7.5	440
H6	3.8	1.5	1.03	1.4	2.9	-0.2	5.9	0.81	0.69	0.56	1.9	0.19	2.4	0.17	6.2	700
H7	3.6	1.4	0.97	3.1	3.9	0.6	5.7	0.77	1.13	1.38	2.5	0.13	1.8	0.13	4.5	390
L1	1.8	2.3	0.94	6.3	6.9	1.6	0.60	0.18	0.20	0.99	1.2	0.37	1.7	0.35	1.6	290

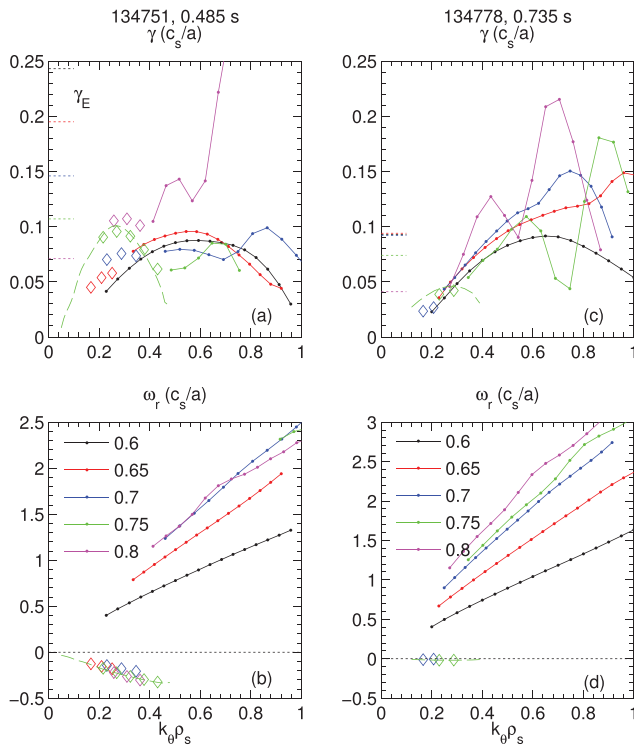


FIG. 1. (a) and (c) Linear growth rate spectra and ((b) and (d)) real frequency spectra at five different radii for NSTX discharges 134751, 0.485 s (left) and 134778, 0.735 s (right), corresponding to cases H1 and H2 in Table I. Solid lines with dots represent microtearing modes. Diamonds represent ballooning parity modes. Dashed lines are the ballooning mode solutions using the GYRO eigenvalue solver. Positive real frequencies correspond to the electron diamagnetic drift direction. The short dotted lines in (a) and (c) are the local $E \times B$ shearing rates as defined in the text.

B. Ballooning mode identification

Subsequent simulations were run varying electron beta for the $k_{\theta}\rho_s = 0.25$ ballooning modes (at $r/a = 0.75$) for the two cases in Fig. 1 to clarify the nature of the instabilities. In the case of 134751, the ballooning mode appears to be an ITG mode (real frequencies in the ion drift direction, $\omega_r < 0$) with a growth rate that is relatively insensitive to beta (see Fig. 2). The onset of a KBM eventually occurs with a $\sim 40\%$ increase in β_e , identified by large real frequencies in the ion direction, a sharp increase in growth rate, and out-of-phase relationship between the real and imaginary components of shear magnetic perturbations (A_{\parallel}).^{30,50} For 134778, the unstable mode has a clear threshold for beta $\sim 30\%$ below the experimental value. Unlike the KBM, this mode has a very small real frequency, eventually becomes stable at increasing beta, and the real and imaginary components of A_{\parallel} are in-phase. Additional tests illustrate that this mode is sensitive to the presence of compressional magnetic perturbations (which can also contribute non-negligibly to transport, as will be shown below), so we generically refer to it as a compressional ballooning mode.⁵⁰ As beta is increased further in 134778, the onset of KBM is apparent as a separate unstable mode with a threshold occurring just above the experimental beta. The remaining H-mode discharges in Table I show similar behavior as the two cases here. We use these two discharges to investigate the predicted momentum

transport from these three types of instabilities (ITG, compressional ballooning, KBM) in the remainder of this section.

As shown in Fig. 1, the sub-dominant ITG mode in 134751 is apparent at low $k_{\theta}\rho_s$ for a number of radii when using the initial value solver (which can only identify the fastest growing mode). In 134778, the compressional modes only appeared at two radii. To help verify the radial extent over which these modes occur, the GYRO eigenvalue solver was used to track the $k_{\theta}\rho_s = 0.25$ ballooning mode across many radii in the measurement region. Fig. 2 shows that both the ITG and compressional modes (in 134751 and 134778, respectively) extend over the entire analysis region ($r/a = 0.6-0.8$). In addition to being weaker than the microtearing modes (seen in Fig. 1), Fig. 2(a) also shows that the ballooning modes also tend to be smaller than the local $E \times B$ shearing rates over most of the analysis region. This brings into question as to whether these sub-dominant ballooning modes would survive in a nonlinear turbulence simulation to contribute to the heat, particle, and momentum fluxes. However, as impurity and ion thermal transport are often close to neoclassical predictions in NSTX,^{28,38,51-53} only a small residual amount of ballooning turbulence may be required to account for the anomalously large momentum transport. We also note that there is a rather large variation in $\gamma_E/\gamma_{\text{lin}}$ over the analysis region which could also imply that finite- ρ_* non-local effects could be important. This will

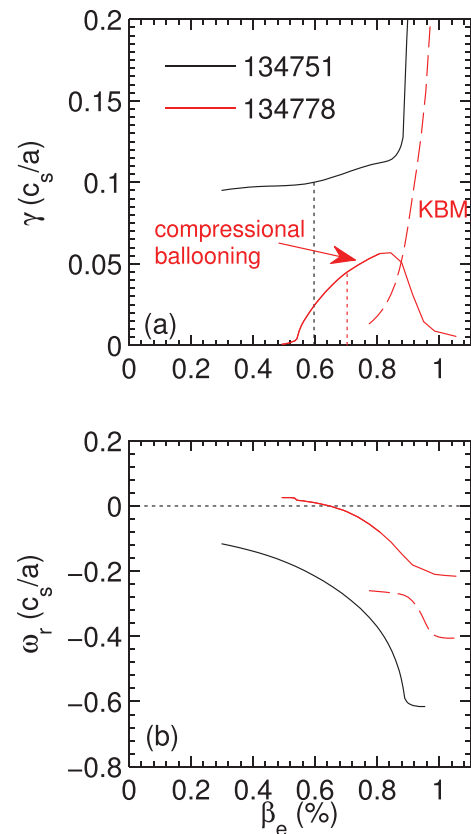


FIG. 2. (a) Linear growth rate and (b) real frequency vs. electron beta for the $r/a = 0.75$, $k_{\theta}\rho_s = 0.25$ ballooning modes in Fig. 1, calculated using the GYRO eigenvalue solver. Vertical dashed lines represent the experimental local values of β_e .

be discussed further in Sec. V. Although these complications are present in the interpretation, in the remainder of this paper we consider only the prediction of Prandtl and momentum pinch from local, quasi-linear simulations of the ballooning modes (assuming that they may contribute in the nonlinear state) to compare with theory that has been developed and validated successfully for conventional aspect ratio tokamaks and gave initial good agreement with NSTX observations.^{27,28}

C. Momentum transport predictions

Ignoring the contribution of any possible residual stresses, the diffusive-convective decomposition of momentum transport (Eq. (1)) can be written nondimensionally using standard gyroBohm normalizations²²

$$\hat{\Pi}_\phi = \sum_i \hat{\Pi}_{\phi,i} = \sum_i \hat{n}_i \hat{m}_i \hat{\chi}_\phi u' + (\hat{n}_i \hat{m}_i \hat{V}_\phi + \hat{m}_i \hat{\Gamma}_{ni}) u, \quad (2)$$

where $\sum_i()$ represents a summation over all ion species, $\hat{\Pi}_{\phi,i} = \Pi_{\phi,i}/(\rho_s^2/R^2 \cdot n_{ref} m_{ref} R c_s)$, $\hat{\chi}_\phi = \chi_\phi/(\rho_s^2 c_s/R)$, $\hat{V}_\phi = V_\phi/(\rho_s^2/R^2 \cdot c_s)$, the normalized particle flux $\hat{\Gamma}_{ni} = \Gamma_{ni}/(\rho_s^2/R^2 \cdot n_{ref} c_s)$, $\hat{m} = m_i/m_{ref}$, and $n_{ref} = n_D$, $m_{ref} = m_D$. We note that with these normalizations, the dimensionless pinch parameter is given by $RV_\phi/\chi_\phi = \hat{V}_\phi/\hat{\chi}_\phi$.

For the discharges in this paper, $Z_{eff} \approx 2-3$ due to carbon which means that carbon carries a significant fraction (20%–40%) of the total angular momentum (for $\Omega_C \approx \Omega_D$ in the limit of strong toroidal rotation applicable in the core of NSTX where poloidal flow and diamagnetic contributions can be ignored). Since the carbon-to-deuterium mass and charge ratios are the same ($m_C/m_D = Z_C = 6$), the total mass in the plasma ($n_D m_D + n_C m_C = n_{ref} m_{ref}$) is constant regardless of Z_{eff} (assuming only fully stripped carbon as the impurity species). However, it will be shown below that the relative diffusive and pinch contributions can be different for the two different species with such large values of Z_{eff} .

To determine the quasi-linear Prandtl number and pinch parameter, we follow the analysis in Refs. 19 and 22, summarized here briefly. Multiple linear simulations are run using different combinations of rotation and rotation gradient, e.g., $[u, u'] = [0, 0], [0, 1], [1, 0], [1, 1] \times [u_{exp}, u'_{exp}]$ (ignoring $E \times B$ shear, $\gamma_E = 0$). From the incremental change in quasi-linear fluxes, we can infer the effective Prandtl number and pinch parameter, e.g.

$$Pr = \frac{\hat{\chi}_\phi}{\hat{\chi}_i} = \frac{(\hat{\Pi}_\phi(0, u') - \hat{\Pi}_\phi(0, 0))}{u'} \cdot \frac{a/L_{Ti}}{\hat{Q}_i}, \quad (3)$$

$$\frac{RV_\phi}{\chi_\phi} = \sum_i \left[\frac{(\hat{\Pi}_{\phi,i}(u, 0) - \hat{\Pi}_{\phi,i}(0, 0))}{u} - \hat{m}_i \hat{\Gamma}_{ni}(u, 0) u \right] \times \frac{u'}{(\hat{\Pi}_\phi(0, u') - \hat{\Pi}_\phi(0, 0))}, \quad (4)$$

where $\hat{Q}_i = Q_i/(\rho_s^2/R^2 \cdot n_{ref} T_{ref} R c_s)$ is the gyroBohm normalized total ion heat flux ($Q_D + Q_C$). To isolate the momentum pinch due to the Coriolis drift, the contribution from

particle convection has been subtracted for each ion species ($\sim m_i \Gamma_{ni} u$).

This method assumes a linear dependence of the momentum flux on rotation and rotation gradient. However, the decomposition of momentum flux into diffusive and convective contributions is an assumption, and the simple linear relationship of Eq. (1) or (2) is not guaranteed from theory.²² While finite rotation tends to have a negligible influence on stability (here we are excluding centrifugal effects, applicable in the low flow limit, $u \ll 1$), sufficiently large values of u' can drive Kelvin-Helmholtz like instability^{54,55} increasing the growth rate and changing the character of the instability. Figs. 3(a) and 3(b) show that for the range of parameters under investigation here, the growth rates are insensitive to changes in u and are increased only a small amount ($\sim 5\%$) for the experimental values of u' , indicating that the dynamics of the unstable ballooning mode is largely unchanged. Figs. 3(c) and 3(d) confirm a nearly linear dependence between momentum flux and rotation and rotation gradient, validating the use of Eqs. (3) and (4) to infer Pr and RV_ϕ/χ_ϕ . In this case, the contribution to the momentum flux is dominated by deuterium ($\Pi_D \sim 3\Pi_C$).

From Figs. 3(c) and 3(d), a number of features about the momentum transport are readily apparent. First, the relative contribution to momentum flux from diffusion $\sim u'$ ($\Pi_\phi \sim 0.7$) is much larger than that due to convection $\sim u$ ($\Pi_\phi \sim 0.07$). In addition, the flux increases with increasing u (Fig. 3(d)), implying an outward momentum convection, in contrast to

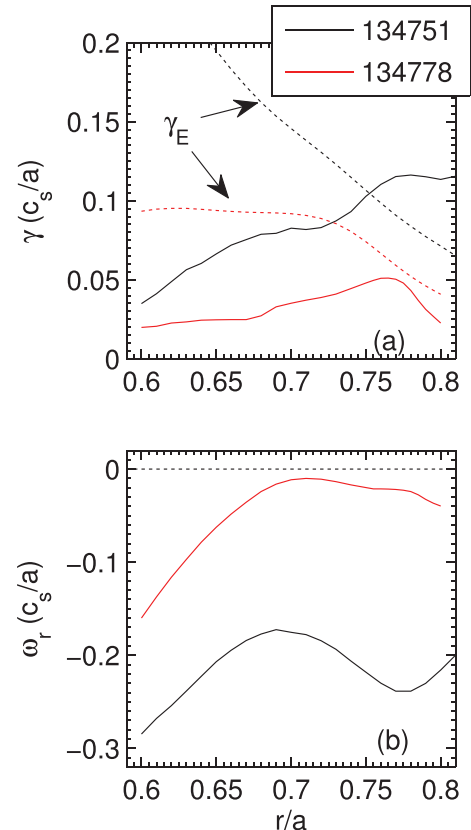


FIG. 3. (a) Linear growth rate and (b) real frequency vs. minor radius for the $k_{\perp} \rho_s = 0.25$ ballooning modes in Fig. 1, calculated using the GYRO eigenvalue solver. The local $E \times B$ shearing rates are given by dashed lines in (a).

the inward convection typically predicted for the Coriolis pinch.²² Finally, a small but finite residual flux is also predicted in the absence of either rotation or rotation gradient ($u = u' = 0$). As these discharges are biased to have a lower single null X-point, and we are using general numerical equilibrium reconstructions (not a model geometry), the flux surfaces are not up-down symmetric allowing for symmetry breaking of the mode structure and the resulting small residual stress contribution.^{56,57} However, the magnitude of this residual stress is considerably smaller than the diffusive contribution. As the analysis method outlined in Eqs. (3) and (4) uses incremental differences in fluxes (i.e., $\Delta\Pi/\Delta u'$, $\Delta\Pi/\Delta u$), this small finite residual stress contribution does not influence the calculation of Prandtl number or pinch parameters.

The resulting Prandtl and pinch parameters for the two cases highlighted above are shown in Fig. 4, plotted vs. $k_\theta \rho_s$. The Prandtl numbers are always less than one, ranging between $Pr = 0.3$ and 0.7 for the wavenumbers where the ballooning modes are predicted to be unstable. This range of Prandtl number was experimentally observed assuming diffusive-only transport in a broad range of NSTX discharges.²⁸ However, as mentioned above, in H-modes the ion thermal transport is often close to neoclassical predictions, implying a small turbulent component ($\chi_{i,\text{exp}} \approx \chi_{i,\text{NC}} \gg \chi_{i,\text{turb}}$), so the concept of a turbulent Prandtl number may be poorly defined. More striking is that the predicted pinch parameter (Fig. 4(b)) is near zero or positive ($RV_\phi/\chi_\phi \approx 0-2$), implying an outward convective momentum flux. This is in contrast to the experimentally inferred inward pinch values ($(RV_\phi/\chi_\phi)_{\text{exp}} = (-1) - (-7)$) inferred from perturbative experiments.²⁷⁻²⁹

Predictions from two additional cases are shown in Fig. 4 as these locations experimentally were experimentally observed to have relatively large inward momentum pinch.

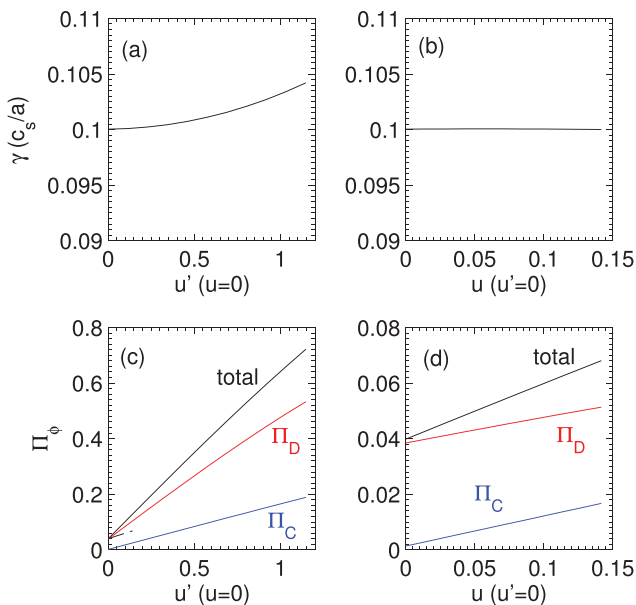


FIG. 4. Linear growth rate of the $k_\theta \rho_s = 0.25$ ballooning mode vs. (a) rotation gradient, u' , and (b) toroidal rotation, u , for discharge 134751 at $r/a = 0.75$. The corresponding quasilinear momentum fluxes are shown in (c) and (d). The particle convection contributions $\sim m_i \Gamma_i u$ have been subtracted in (c) and (d).

However, there is no sign of a predicted strong pinch in any of these cases. Fig. 5 summarizes the comparison of predicted pinch vs. inferred experimental pinch for these three different discharges (134751, 134778, 134779), over the region of interest, illustrating the lack of agreement. This suggests that the Coriolis pinch mechanism does not provide a likely explanation for the measured inward momentum pinch, even though comparisons with analytic theory estimates based on conventional aspect ratio tokamaks^{19,23} appeared to provide a reasonably good explanation.^{27,28}

It has been noted previously that at increasing beta, the predicted inward Coriolis pinch is weakened for ITG turbulence due to electromagnetic effects and can even reverse directions for the KBM.³⁵ To investigate this for the NSTX H-modes, Figs. 6(a) and 6(b) show the corresponding Pr and RV_ϕ/χ_ϕ parameters for the two beta scan cases shown in Fig. 7. For the compressional mode found in 134778, the pinch is always positive (outward). For 134751, which shows a transition from ITG at low beta to KBM at $\beta_e > 0.88\%$, there is a complicated non-monotonic dependence. Most notably, even for the ITG branch at low beta, there is an outward convection ($RV_\phi/\chi_\phi > 0$) that is weakened as the KBM branch is approached. There appears to be only a very small range of

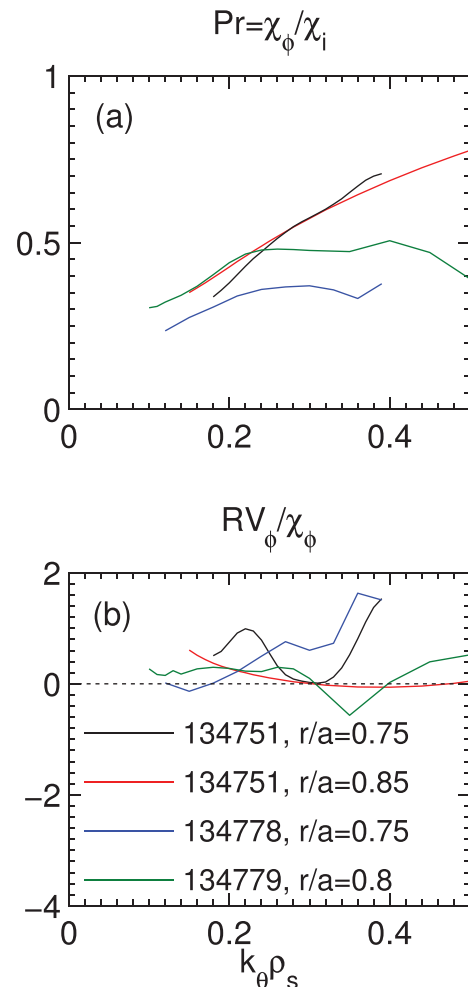


FIG. 5. (a) Prandtl number and (b) pinch parameter from local, quasi-linear predictions for the ITG and electromagnetic ballooning modes in various discharges.

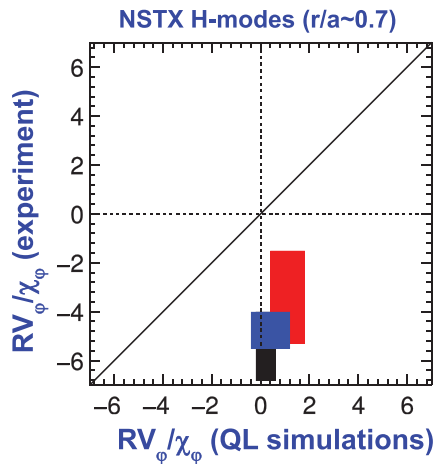


FIG. 6. Comparison of experimentally measured vs. predicted momentum pinch parameter, RV_ϕ/χ_ϕ for three NSTX H-mode discharges: (black) 134 751, (red) 134 778, and (blue) 134 779.

beta where a negligibly small inward pinch is predicted. Once the KBM is unstable, the outward convection is again weakened with increasing beta.

At this point, we attempt to draw a connection between previous analytic theory and the current simulations that show negligible or outward momentum pinch. Much physical insight has been gained about the Coriolis momentum pinch through the use of a fluid model for a pure deuterium, electrostatic ITG instability, evaluated at the low field side ($\theta=0$) of a low beta, and circular flux surface equilibrium.^{19–21} While this model is far too simple to interpret the calculations here (fully electromagnetic at high beta, using shaped flux surfaces at low-aspect-ratio and multiple kinetic

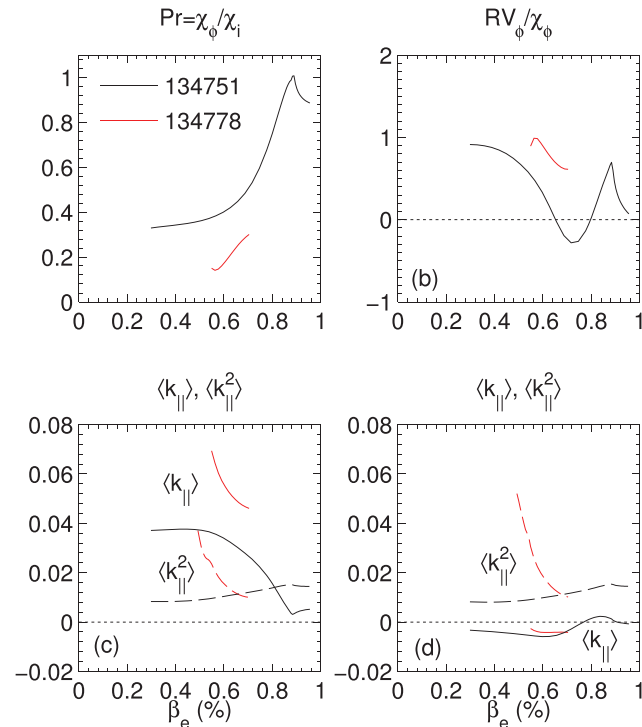


FIG. 7. (a) Pr and (b) RV_ϕ/χ_ϕ for the beta scan shown in Fig. 2. The corresponding $\langle k_{\parallel} \rangle$ (solid line) and $\langle k_{\parallel}^2 \rangle$ (dashed line) is shown for (c) finite u' ($u=0$) and (d) finite u ($u'=0$).

ion species), a few noteworthy observations can still be made. First, a portion of the Coriolis pinch comes into effect through a term that depends linearly on both the finite toroidal flow and the parallel mode structure, $\sim(2 \cdot k_{\theta} \rho_s / R \cdot u + k_{\parallel}) \delta v_{\parallel}$ (where δv_{\parallel} is the perturbed parallel fluid velocity). If the parallel mode structure is ignored completely ($k_{\parallel}=0$), the pinch in the low-field-side fluid model is given by $RV_\phi/\chi_\phi = -4 - R/L_n$.¹⁹ However, in the limit of adiabatic electrons with finite flow (in the absence of any other symmetry breaking effects), the parallel mode structure of the most unstable mode occurs for a finite k_{\parallel} that it exactly balances the flow term such that no pinch occurs (referred to as the compensation effect²¹). Alternatively, if the presence of (non-adiabatic) trapped electrons is considered, they tend to keep the mode more closely centered on the outboard midplane ($\theta=0$), keeping the average k_{\parallel} closer to zero, preventing a complete compensation, and allowing for a finite pinch which increases with trapped particle fraction. Fig. 6(d) shows that the normalized averaged parallel wavenumber $k_{\parallel,N} = \langle k_{\parallel} \rangle \cdot R / (2 \cdot k_{\theta} \rho_s)$ of the mode structure in these H-mode cases remains relatively small (presumably due to significant fraction of trapped electrons) in comparison to the toroidal flow ($u=0.14$), indicating that the compensation effect has been weakened significantly. This would suggest that a strong inward pinch could develop.

However, in addition to the dependence on k_{\parallel} (indicative of the degree of asymmetry at the outboard midplane for a ballooning mode), the predicted pinch also depends on the parallel mode structure through a dependence on $\langle k_{\parallel}^2 \rangle$. In the limit of $k_{\parallel,N} \ll u$ (satisfied in these cases), the pinch term in the local, low-field-side fluid theory becomes $(RV_\phi/\chi_\phi) \approx (-4 - R/L_n + 12 k_{\parallel,N}^2)$.²⁰ Therefore, if the parallel mode structure becomes strongly localized (large $k_{\parallel,N}^2$), the pinch can be weakened dramatically or even reverse sign. Fig. 6(d) shows that $\langle k_{\parallel,N}^2 \rangle$ can be comparable to or larger than $\langle k_{\parallel,N} \rangle$, which coincides where the pinch is weak or outward, loosely following this trend. For comparison, in the case of finite u' , Fig. 6(c) shows that the average $k_{\parallel,N}$ tends to be much larger than $k_{\parallel,N}^2$; i.e., the toroidal flow shear is much more effective at breaking the symmetry of the instabilities, which leads to the resulting diffusive transport. While the simple fluid theory cannot capture the complicated dependence observed, it qualitatively illustrates the role of the parallel mode structure on the pinch.

Before moving on we also wish to note that for these high beta plasmas, the contribution to momentum fluxes is not always dominated by electrostatic fluctuations. Fig. 8 shows the contributions to both deuterium and carbon momentum flux (for finite u' , $u=0$) from electrostatic (φ), shear magnetic (A_{\parallel}), and compressional magnetic (B_{\parallel}) fluctuations. In the case of 134 751 (Figs. 8(a) and 8(b)), the flux is dominated by electrostatic fluctuations over a range of beta, even as the KBM becomes dominant above $\beta_e > 0.88\%$. However, for 134 778 (Figs. 8(c) and 8(d)), there are substantial contributions from the compressional magnetic perturbations, confirming the compressional nature of this instability as discussed above and mentioned in previous ST studies.^{30,50,58} Fig. 8 also shows that the relative contribution of carbon to the momentum flux is different in the two

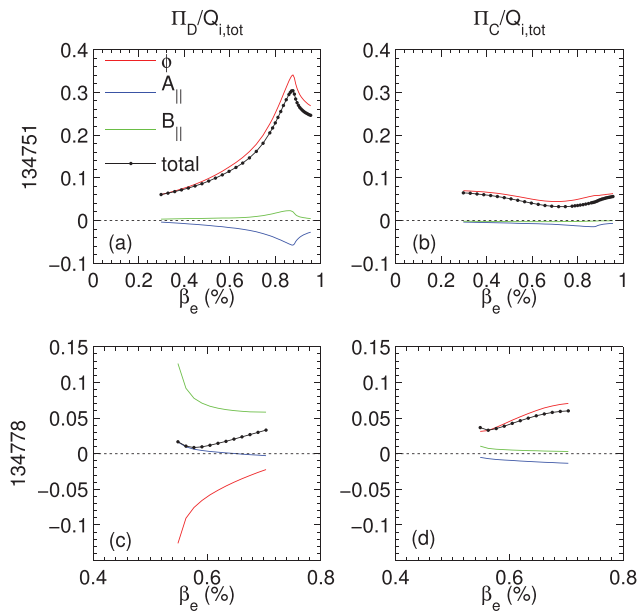


FIG. 8. Contributions to momentum flux (with finite u') from electrostatic (ϕ), shear magnetic ($A_{||}$) and compressional magnetic ($B_{||}$) fluctuations, for (a) and (c) deuterium and (b) and (d) carbon species. Fluxes are shown for the beta scan of Figs. 2 and 6 (top) 134 751, (bottom) 134 778.

discharges and can vary with beta. Furthermore, the relative contribution of deuterium and carbon flux to Pr and RV/χ_ϕ can vary. For example in the case of 134 778, deuterium contributes more to the diffusive transport (χ_ϕ), while carbon contributes more to the convective transport (V_ϕ).

IV. L-MODE RESULTS

As the high beta NSTX H-mode discharges are predicted to be unstable to a mix of electrostatic and electromagnetic modes (MTM with weaker ITG and compressional modes, often near KBM limits), additional simulations were run for an NSTX L-mode discharge (parameters listed in Tables I and II) at reduced beta to determine whether an inward momentum pinch is predicted for experimentally realizable lower beta discharges, more consistent with theory for a conventional aspect ratio. The outer half region of this plasma is unstable to traditional electrostatic ITG-TEM turbulence, based on local gyrokinetic analysis as discussed in Ref. 59. We also note that the impurity content is very low in this plasma ($Z_{\text{eff}} \sim 1.2$) compared to the H-mode plasmas and the influence of carbon on momentum transport is negligible. These conditions are much closer to those used in the fluid modeling^{19–21} discussed above and simplify the theoretical interpretation compared to the H-mode plasmas, although no experimental measurements of momentum pinch are available for the L-mode case.

Fig. 9 shows the Prandtl and pinch number spectra at a number of radii in the NSTX L-mode, calculated using the local, quasi-linear gyrokinetic analysis described in Section III. The Prandtl number increases from small values at low $k_\theta \rho_s$ to over unity at increasing $k_\theta \rho_s$. Local, nonlinear simulations for this case have also been run (reported in Ref. 59), indicating that the nonlinear flux spectra peak around

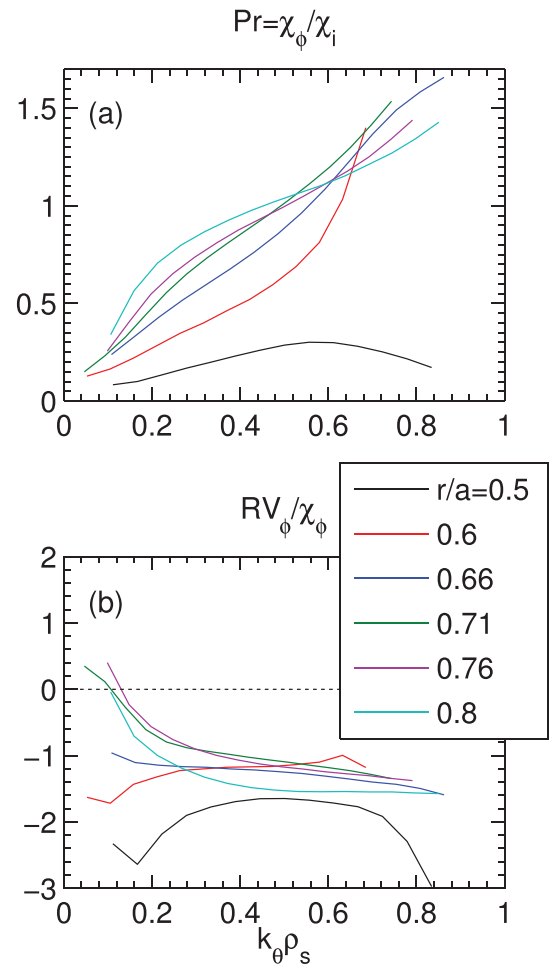


FIG. 9. (a) Prandtl and (b) pinch parameter vs. $k_\theta \rho_s$ for a number of radii in NSTX L-mode 141 716.

$k_\theta \rho_s = 0.3$. For this wavenumber, the Prandtl number ranges between 0.2 and 0.8, which falls in the range of the experimental Prandtl numbers (assuming purely diffusive flux). In contrast to the H-mode results above, the predicted pinch parameter (Fig. 8(b)) is now always inward directed and varies between $RV_\phi/\chi_\phi = (-1) - (-2)$. This inward pinch is more consistent with that observed and predicted in conventional tokamaks, although limited to relatively small magnitude.

Fig. 10 shows the results of a beta scan at $r/a = 0.6$ for this L-mode to connect with the results discussed in the H-mode analyses. It can be seen that locally the experimental values of beta are well below the onset of KBM instability, although there is a smooth, continuous transition between the low beta ITG-TEM modes and the KBM instability indicative of the “hybrid-KBM” behavior discussed elsewhere.^{30,50} We note that although the real frequencies are in the ion drift direction even at low beta ($\omega_r < 0$ in Fig. 10(a)), the modes behave with both ITG and TEM characteristics in that they are driven unstable by electron and ion temperature gradients as well as the density gradient. Similar to the H-modes, the growth rates at these locations are also found to be insensitive to the experimental values of u and u' . The resulting Prandtl number does not vary significantly, while the pinch parameter is reduced in magnitude as beta is increased, approaching zero although never quite becoming

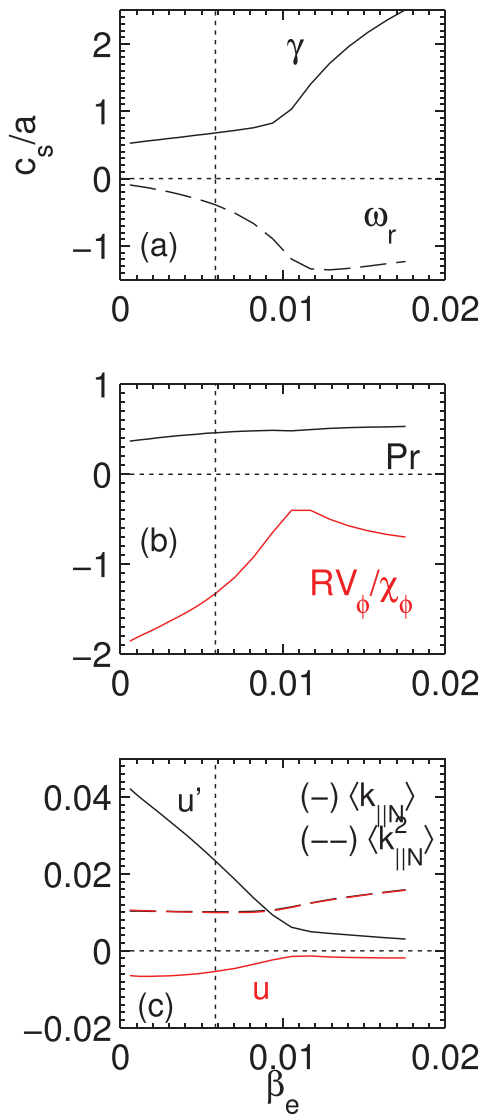


FIG. 10. (a) Growth rate (solid line) and real frequency (dashed line), (b) Prandtl number (black line) and pinch parameter (red line), and (c) $k_{\parallel,N}$ (solid line) and $k_{\parallel,N}^2$ (dashed line) for finite u' (black) and u (red), calculated for NSTX L-mode 141 716, ITG/TEM ballooning mode at $r/a=0.6$ and $k_{\theta}\rho_s=0.3$. Vertical lines represent the experimental value of β_e .

positive (outward) as the KBM branch is reached. For the case of finite $u=0.4$, $k_{\parallel,N}$ is relatively small ($\ll u$) and decreasing with beta while $k_{\parallel,N}^2$ is slightly increasing. These conditions are similar to those in the H-modes above, suggesting that the parallel mode structure similarly influences the pinch for the low beta ITG-TEM instability in NSTX.

Additional parameter scans have been run to identify if ranges exist where a large inward pinch would be predicted for the ITG-TEM modes at low aspect ratio. Scans over safety factor, magnetic shear, electron or ion temperature gradient, and collision frequency all show very weak dependencies. From theoretical analysis^{19,20,22} as well as multiple experimental observations,^{16–18,26} the influence of the local density gradient (R/L_n) has been predicted to be significant, with a proportionality $RV_{\phi}/\chi_{\phi} \sim -C_{\nabla n} R/L_n$ ranging between $C_{\nabla n}=(0.4-1.2)$. Fig. 11 shows that there is very little sensitivity of the predicted pinch to density gradient for

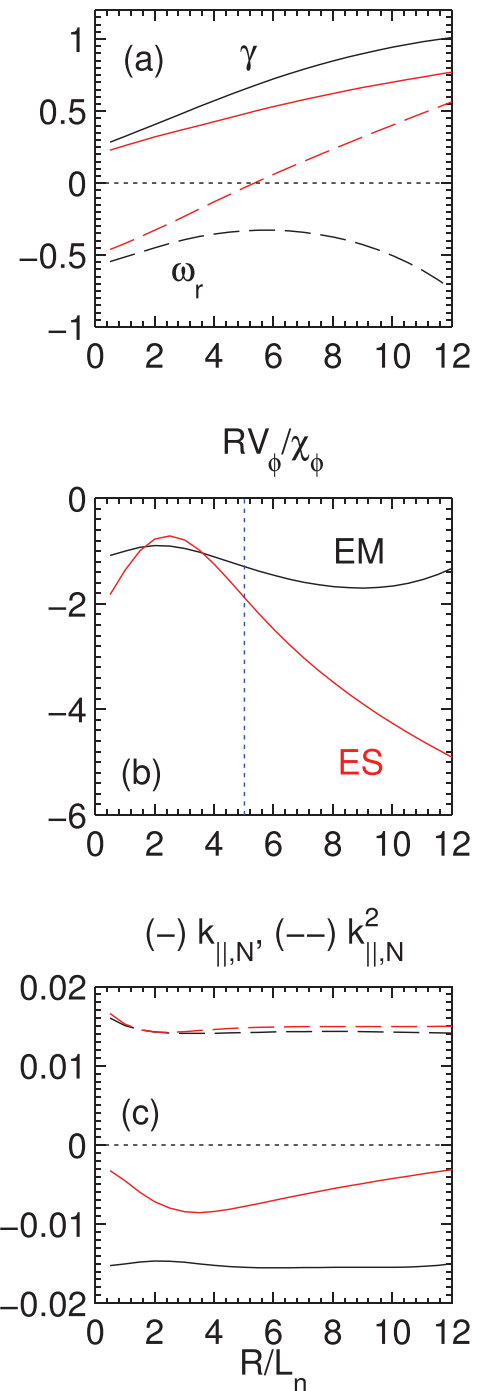


FIG. 11. (a) Growth rate (solid line) and real frequency (dashed line), (b) pinch parameter, and (c) $k_{\parallel,N}$ (solid line) and $k_{\parallel,N}^2$ (dashed line) vs. density gradient (R/L_n) for the NSTX L-mode 141 716 at $r/a=0.6$ ($k_{\theta}\rho_s=0.3$). Both electromagnetic (at experimental $\beta_e=0.6\%$) and electrostatic ($\beta_e=0$) predictions are shown. (Vertical line indicates experimental value of R/L_n .)

the experimental case over a broad range of R/L_n . However, if the density scan is repeated in the purely electrostatic limit ($\beta_e \rightarrow 0$), a stronger inward pinch is predicted at increased density gradient, with a proportionality that is similar to conventional aspect ratio tokamaks, $C_{\nabla n} \approx 0.5$, for $R/L_n > 3$. In this case, there is very little change in parallel mode structure when going from electromagnetic to electrostatic, and if anything there is a further decrease in $k_{\parallel,N}$ relative to $k_{\parallel,N}^2$ in the

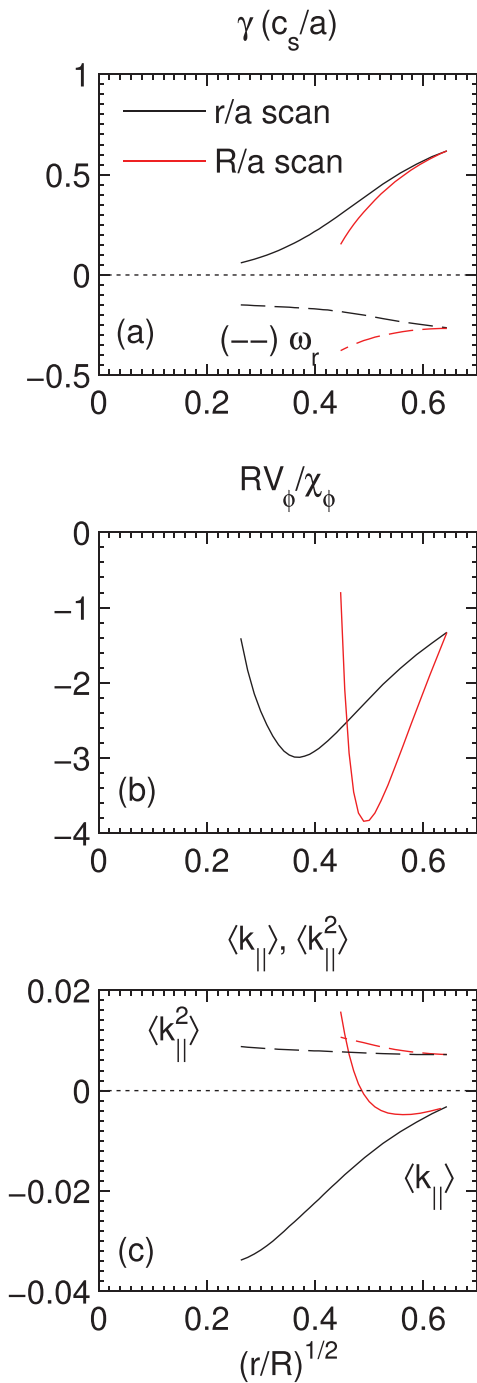


FIG. 12. (a) Linear growth rate, (b) pinch parameter, and (c) average k_{\parallel} vs. $(r/R)^{1/2}$ as a proxy for trapped particle fraction for the NSTX L-mode 141 716 at $r/a = 0.6$ ($k_{\theta}\rho_s = 0.3$). Two separate scans are shown varying flux surface (r/a) for a fixed aspect ratio, and varying aspect ratio (R/a) for a fixed flux surface (see text for description).

electrostatic case at larger density gradient where a strong inward pinch is eventually recovered. We speculate that the change in real frequency that occurs over this range of parameters may also influence the strength of the pinch, as discussed in Ref. 35.

As there is a very large fraction of trapped particles $\sim (r/R)^{1/2}$ in these low aspect ratio discharges, it is of interest to investigate how the predicted pinch varies with minor radius or aspect ratio. To accomplish this, two different scans

were run using a local equilibrium expansion⁶⁰ that keep all other shaping and equilibrium parameters constant (as opposed to recalculating self-consistent global equilibria, e.g., as done in Ref. 61). In the first scan, only the minor radius of the flux surface is varied, which has the largest effect of changing the strength of the $|B(\theta)|$ ripple and corresponding particle trapping, with a weaker variation in $\nabla B/\text{curvature}$ drifts and local magnetic shear. In the second scan, the aspect ratio was varied (a/R) while keeping the normalized flux surface (r/a) unchanged. While this approach similarly varies $|B(\theta)|$ and particle trapping, it also causes a larger variation to the $\nabla B/\text{curvature}$ drifts and local magnetic shear which can strongly influence stability (and is presumably more consistent with transitioning from low aspect ratio to high aspect ratio global equilibria).

Fig. 12(a) shows that the growth rates of the ITG/TEM instability are weakened as particle trapping is reduced, illustrating the importance of the trapped electrons to mode growth. Fig. 12(b) shows that the corresponding pinch parameter exhibits a surprising non-monotonic dependence on $(r/R)^{1/2}$. Increasing from the lowest particle trapping (small r/a , or large R/a) enhances the influence of the trapped electrons, which minimizes the “compensation” effect,²¹ allowing for a stronger pinch. This is confirmed by a decrease in the magnitude of $k_{\parallel N}$ in both scans Fig. 12(c). However, this trend is eventually reversed with a decrease in pinch occurring for further increasing trapping. We speculate that as $k_{\parallel N}$ becomes smaller, the influence of the nearly constant $k_{\parallel N}^2$ becomes relatively more important leading to the weakening of the pinch as discussed above.

V. DISCUSSION AND SUMMARY

The gyrokinetic analysis presented in this paper was motivated by measurements of an inward momentum pinch in NSTX H-modes and the encouraging agreement with early theory developed for ITG turbulence at conventional aspect ratio.^{27,28} However, linear gyrokinetic simulations based on the experimental NSTX H-mode profile and equilibrium data predict instability mechanisms that are not common in the core of conventional tokamaks. In all seven H-modes analyzed, electromagnetic microtearing modes are predicted to be the strongest unstable modes over a wide range of wavenumbers ($k_{\theta}\rho_s \leq 1$) in the region of interest ($\rho = 0.5-0.7$). In all cases, there are weaker, sub-dominant ballooning modes that are also present. Using the GYRO eigenvalue solver, these modes tend to peak at lower wavenumbers ($k_{\theta}\rho_s \sim 0.2-0.3$) and to exhibit a variety of behavior. Although electrostatic ITG modes are present in some cases, many of the modes are electromagnetic with a threshold in beta. The electromagnetic modes are identified as compressional ballooning modes (depending on compressional magnetic perturbations with a non-monotonic beta dependence), and more traditional kinetic ballooning modes.

As microtearing modes only give rise to electron thermal transport, local quasi-linear predictions of momentum pinch have been calculated for the weaker ballooning modes, assuming that they can contribute transport nonlinearly (which will be investigated in future nonlinear simulations).

For H-modes, the simulations predict very weak, or even outward, momentum convection with a pinch parameter ranging between $RV_{\phi}/\chi_{\phi} = 0-2$, for both electrostatic and electromagnetic ballooning modes. This prediction is in contrast with the measurements where $RV_{\phi}/\chi_{\phi} = (-1)-(-7)$ were found.^{27,28} These predictions are also apparently at odds with the early theoretical predictions of momentum pinch for ITG turbulence that give $RV_{\phi}/\chi_{\phi} = -4 - R/L_n$ ¹⁹ or -4 .²³ However, later theoretical investigations demonstrated how trapped electron and electromagnetic effects influence the parallel mode structure can ultimately weaken the momentum pinch.^{35,45} Our investigations suggest that this is an important element describing the weak or outward predicted momentum pinch in low aspect ratio, high beta NSTX H-modes.

Additional simulations for a low beta NSTX L-mode, unstable to more traditional electrostatic ITG-TEM instability, indicate an inward pinch that was also relatively weak, $RV_{\phi}/\chi_{\phi} \sim (-1)-(-2)$, and insensitive to variation in most parameters investigated. However, two cases were identified where a larger inward pinch was recovered. In the first case, a stronger scaling with density gradient is recovered, $RV_{\phi}/\chi_{\phi} \sim -0.5R/L_n$, but only in the purely electrostatic limit. Second, if the trapped particle fraction is decreased (either by reducing r/a or increasing aspect ratio R/a), a stronger inward pinch can be recovered, although this effect is non-monotonic. These complicated dependencies appear to be at least partially correlated with how the resulting parallel mode structure is influenced.

As the Coriolis effect (evaluated in the local limit) does not explain the observed momentum pinch in NSTX H-modes, we briefly consider other mechanisms that may be important. As discussed in recent reviews,^{10,22} the various physical mechanisms that cause momentum transport can be identified by how they break parallel and/or radial symmetry of the unstable modes. For example, while $E \times B$ shearing can suppress turbulent transport, it can also tilt eddies, breaking their radial and parallel symmetry, thereby causing a momentum flux.⁶² However, it was shown in nonlinear simulations⁶³ that this contribution becomes small for $E \times B$ shearing rates comparable to linear growth rates, which is similar to what is found in these NSTX plasmas (Fig. 3). Up-down flux surface asymmetry can also lead to a residual stress momentum flux;^{56,57} however, this was directly predicted to be relatively small for these NSTX cases (Fig. 4 and discussion). While centrifugal effects on momentum transport are not predicted to be substantial in the fluid modeling,²⁰ recent gyrokinetic simulations for related NSTX H-modes found that they can provide a contribution comparable to the Coriolis pinch.⁶⁴ This effect will be investigated further in future simulations. There are also a number of finite- ρ_* effects that could lead to symmetry breaking and contribute to the momentum flux. These are particularly interesting given the relatively larger values of $\rho_* = \rho_i/a \sim 1/100$ found in NSTX H-modes (Table I). These effects include profile shearing of eddies due to radial variations in mode frequency or $E \times B$ shearing rate (shown in Fig. 3 over the region $r/a = 0.6-0.8$ corresponding to a physical radial extent $L_r \approx 20-30 \rho_s$),^{65,66} profile variation in the non-linear

turbulence intensity,⁶⁷ and neoclassical flows.⁶⁸⁻⁷⁰ These effects will also be investigated in future simulations. Finally, we note that the experimental interpretation of the perturbative momentum transport experiments would need to be revisited if any of these effects are expected to be important.

ACKNOWLEDGMENTS

We would like to thank C. Angioni, Y. Camenen, and T. Tala for useful discussions. This work was funded by DOE Contract No. DE-AC02-09CH11466. The digital data for this paper can be found at <http://arks.princeton.edu/ark:/88435/dsp0137720g13x>.

- ¹A. Bondeson and D. Ward, *Phys. Rev. Lett.* **72**, 2709 (1994).
- ²E. J. Strait, T. S. Taylor, A. D. Turnbull, J. R. Ferron, L. L. Lao, B. Rice, O. Sauter, S. J. Thompson, and D. Wróblewski, *Phys. Rev. Lett.* **74**, 2483 (1995).
- ³S. A. Sabbagh, J. W. Berkery, R. E. Bell, J. M. Bialek, S. P. Gerhardt, J. E. Menard, R. Betti, D. A. Gates, B. Hu, O. N. Katsuro-Hopkins, B. P. LeBlanc, F. M. Levinton, J. Manickam, K. Tritz, and H. Yuh, *Nucl. Fusion* **50**, 025020 (2010).
- ⁴J. W. Berkery, S. A. Sabbagh, R. Betti, B. Hu, R. E. Bell, S. P. Gerhardt, J. Manickam, and K. Tritz, *Phys. Rev. Lett.* **104**, 035003 (2010).
- ⁵H. Biglari, P. H. Diamond, and P. Terry, *Phys. Fluids B* **2**, 1 (1990).
- ⁶R. E. Waltz, G. D. Kerbel, and J. Milovich, *Phys. Plasmas* **1**, 2229 (1994).
- ⁷K. H. Burrell, *Phys. Plasmas* **4**, 1449 (1997).
- ⁸P. W. Terry, *Rev. Mod. Phys.* **72**, 109 (2000).
- ⁹A. E. White, N. T. Howard, M. Greenwald, M. L. Reinke, C. Sung, S. Baek, M. Barnes, J. Candy, A. Dominguez, D. Ernst, C. Gao, A. E. Hubbard, J. W. Hughes, Y. Lin, D. Mikkelsen, F. Parra, M. Porkolab, J. E. Rice, J. Walk, S. J. Wukitch, and the Alcator C-Mod Team, *Phys. Plasmas* **20**, 056106 (2013).
- ¹⁰C. Angioni, *Plasma Fusion Res.* **8**, 2102032 (2013).
- ¹¹N. Mattor and P. H. Diamond, *Phys. Fluids* **31**, 1180 (1988).
- ¹²S. D. Scott, P. H. Diamond, R. J. Fonck, R. J. Goldston, R. B. Howell, K. P. Jaehrig, G. Schilling, E. J. Synakowski, M. C. Zarnstorff, C. E. Bush, E. Fredrickson, K. W. Hill, A. C. Janos, D. K. Mansfield, D. K. Owens, H. Park, G. Pautasso, A. T. Ramsey, J. Schivell, G. D. Tait, W. M. Tang, and G. Taylor, *Phys. Rev. Lett.* **64**, 531 (1990).
- ¹³K. Ida and J. E. Rice, *Nucl. Fusion* **54**, 045001 (2014).
- ¹⁴P. H. Diamond, *Nucl. Fusion* **53**, 104019 (2013).
- ¹⁵M. Yoshida, S. Kaye, J. Rice, W. Solomon, T. Tala, R. E. Bell, K. H. Burrell, J. Ferreira, Y. Kamada, D. McDonald, P. Mantica, Y. Podpaly, M. L. Reinke, Y. Sakamoto, A. Salmi, and the ITPA Transport and Confinement Topical Group, *Nucl. Fusion* **52**, 123005 (2012).
- ¹⁶T. Tala, A. Salmi, C. Angioni, F. J. Casson, G. Corrigan, J. Ferreira, C. Giroud, P. Mantica, V. Naulin, and A. G. Peeters, *Nucl. Fusion* **51**, 123002 (2011).
- ¹⁷H. Weisen, Y. Camenen, A. Salmi, T. W. Versloot, P. C. de Vries, M. Maslov, T. Tala, M. Beurskens, C. Giroud, and JET-EFDA contributors, *Nucl. Fusion* **52**, 042001 (2012).
- ¹⁸H. Weisen, Y. Camenen, A. Salmi, T. W. Versloot, P. C. de Vries, M. Maslov, T. Tala, M. Beurskens, C. Giroud, and JET-EFDA contributors, *Nucl. Fusion* **52**, 114024 (2012).
- ¹⁹A. G. Peeters, C. Angioni, and D. Strintzi, *Phys. Rev. Lett.* **98**, 265003 (2007).
- ²⁰A. G. Peeters, D. Strintzi, Y. Camenen, C. Angioni, F. J. Casson, W. A. Hornsby, and A. P. Snodi, *Phys. Plasmas* **16**, 042310 (2009).
- ²¹A. G. Peeters, C. Angioni, Y. Camenen, F. J. Casson, W. A. Hornsby, A. P. Snodi, and D. Strintzi, *Phys. Plasmas* **16**, 062311 (2009).
- ²²A. G. Peeters, C. Angioni, A. Bortolon, Y. Camenen, F. J. Casson, B. Duval, L. Fiederspiel, W. A. Hornsby, Y. Idomura, T. Hein, N. Kluy, P. Mantica, F. I. Parra, A. P. Snodin, G. Szepesi, D. Strintzi, T. Tala, G. Tardini, P. de Vries, and J. Weiland, *Nucl. Fusion* **51**, 094027 (2011).
- ²³T. S. Hahm, P. H. Diamond, O. D. Gurcan, and G. Rewoldt, *Phys. Plasmas* **14**, 072302 (2007).
- ²⁴T. S. Hahm, P. H. Diamond, O. D. Gurcan, and G. Rewoldt, *Phys. Plasmas* **15**, 055902 (2008).

- ²⁵T. S. Hahm, J. Lee, W. X. Wang, P. H. Diamond, G. J. Choi, D. H. Na, K. J. Chung, and Y. S. Hwang, *Nucl. Fusion* **54**, 123012 (2014).
- ²⁶T. Tala, R. M. McDermott, J. E. Rice, A. Salmi, W. Solomon, C. Angioni, C. Gao, C. Giroud, W. Guttenfelder, J. Ferreira, S. Kaye, P. Mantica, Y. Podpaly, F. Rytter, G. Tardini, M. Yoshida, JET-EFDA contributors, the ASDEX-Upgrade team, the DIII-D team, the C-Mod team, the NSTX team, and the ITPA Transport and Confinement Topical group, "Tokamak experiments to study the parametric dependence of momentum transport," in *Proceedings of the IAEA Fusion Energy Conference*, San Diego, CA, 2012, No. IAEA-FEC ITR/P1-19.
- ²⁷W. Solomon, S. M. Kaye, R. E. Bell, B. P. LeBlanc, J. E. Menard, G. Rewoldt, W. Wang, F. M. Levinton, H. Yuh, and S. A. Sabbagh, *Phys. Rev. Lett.* **101**, 065004 (2008).
- ²⁸S. M. Kaye, W. Solomon, R. E. Bell, B. P. LeBlanc, F. Levinton, J. Menard, G. Rewoldt, S. Sabbagh, W. Wang, and H. Yuh, *Nucl. Fusion* **49**, 045010 (2009).
- ²⁹W. M. Solomon, K. H. Burrell, A. M. Garofalo, S. M. Kaye, R. E. Bell, A. J. Cole, J. S. deGrassie, P. H. Diamond, T. S. Hahm, G. L. Jackson, M. J. Lanctot, C. C. Petty, H. Reimerdes, S. A. Sabbagh, E. J. Strait, T. Tala, and R. E. Waltz, *Phys. Plasmas* **17**, 056108 (2010).
- ³⁰W. Guttenfelder, J. L. Peterson, J. Candy, S. M. Kaye, Y. Ren, R. E. Bell, G. W. Hammett, B. P. LeBlanc, D. R. Mikkelsen, W. M. Nevins, and H. Yuh, *Nucl. Fusion* **53**, 093022 (2013).
- ³¹W. Guttenfelder, J. Candy, S. M. Kaye, W. M. Nevins, E. Wang, R. E. Bell, G. W. Hammett, B. P. LeBlanc, D. R. Mikkelsen, and H. Yuh, *Phys. Rev. Lett.* **106**, 155004 (2011).
- ³²W. Guttenfelder, J. Candy, S. M. Kaye, W. M. Nevins, E. Wang, J. Zhang, R. E. Bell, N. A. Crocker, G. W. Hammett, B. P. LeBlanc, D. R. Mikkelsen, Y. Ren, and H. Yuh, *Phys. Plasmas* **19**, 056119 (2012).
- ³³H. Doerk, F. Jenko, M. J. Pueschel, and D. R. Hatch, *Phys. Rev. Lett.* **106**, 155003 (2011).
- ³⁴H. Doerk, F. Jenko, T. Görler, D. Told, M. J. Pueschel, and D. R. Hatch, *Phys. Plasmas* **19**, 055907 (2012).
- ³⁵T. Hein, C. Angioni, E. Fable, J. Candy, and A. G. Peeters, *Phys. Plasmas* **18**, 072503 (2011).
- ³⁶S. M. Kaye, R. E. Bell, D. Gates, B. P. LeBlanc, F. M. Levinton, J. E. Menard, D. Mueller, G. Rewoldt, S. A. Sabbagh, W. Wang, and H. Yuh, *Phys. Rev. Lett.* **98**, 175002 (2007).
- ³⁷S. M. Kaye, F. M. Levinton, D. Stutman, K. Tritz, H. Yuh, M. G. Bell, R. E. Bell, C. W. Domier, D. Gates, W. Horton, J. Kim, B. P. LeBlanc, N. C. Luhmann, Jr., R. Maingi, E. Mazzucato, J. E. Menard, D. Mikkelsen, D. Mueller, H. Park, G. Rewoldt, S. A. Sabbagh, D. R. Smith, and W. Wang, *Nucl. Fusion* **47**, 499 (2007).
- ³⁸S. M. Kaye, S. Gerhardt, W. Guttenfelder, R. Maingi, R. E. Bell, A. Diallo, B. P. LeBlanc, and M. Podesta, *Nucl. Fusion* **53**, 063005 (2013).
- ³⁹J. Candy and R. E. Waltz, *Phys. Rev. Lett.* **91**, 045001 (2003).
- ⁴⁰J. Candy and R. E. Waltz, *J. Comput. Phys.* **186**, 545 (2003).
- ⁴¹J. Candy and E. Belli, General Atomics Technical Report No. GA-A26818 (2010).
- ⁴²See <http://nstx-u.pppl.gov/software/lrdfit> for a description of the LRDFIT code.
- ⁴³F. M. Levinton and H. Yuh, *Rev. Sci. Instrum.* **79**, 10F522 (2008).
- ⁴⁴B. P. LeBlanc, R. E. Bell, D. W. Johnson, D. E. Hoffman, D. C. Long, and R. W. Palladino, *Rev. Sci. Instrum.* **74**, 1659 (2003).
- ⁴⁵N. Kluy, C. Angioni, Y. Camenen, and A. G. Peeters, *Phys. Plasmas* **16**, 122302 (2009).
- ⁴⁶J. Candy, *Plasma Phys. Controlled Fusion* **51**, 105009 (2009).
- ⁴⁷R. E. Bell and R. Feder, *Rev. Sci. Instrum.* **81**, 10D724 (2010).
- ⁴⁸W. Guttenfelder, J. Candy, S. M. Kaye, W. M. Nevins, R. E. Bell, G. W. Hammett, B. P. LeBlanc, and H. Yuh, *Phys. Plasmas* **19**, 022506 (2012).
- ⁴⁹S. M. Kaye, W. Guttenfelder, R. E. Bell, S. P. Gerhardt, B. P. LeBlanc, and R. Maingi, *Phys. Plasmas* **21**, 082510 (2014).
- ⁵⁰E. A. Belli and J. Candy, *Phys. Plasmas* **17**, 112314 (2010).
- ⁵¹L. Delgado-Aparicio, D. Stutman, K. Tritz, M. Finkenthal, S. Kaye, R. E. Bell, R. Kaita, B. LeBlanc, F. Levinton, and J. Menard, *Nucl. Fusion* **49**, 085028 (2009).
- ⁵²L. Delgado-Aparicio, D. Stutman, K. Tritz, F. Volpe, K. L. Wong, R. E. Bell, M. Finkenthal, E. Fredrickson, S. P. Gerhardt, and S. Kaye, *Nucl. Fusion* **51**, 083047 (2011).
- ⁵³F. Scotti, V. A. Soukhanovskii, R. E. Bell, S. Gerhardt, W. Guttenfelder, S. Kaye, R. Andre, A. Diallo, R. Kaita, B. P. LeBlanc, M. Podesta, and the NSTX Team, *Nucl. Fusion* **53**, 083001 (2013).
- ⁵⁴P. J. Catto *et al.*, *Phys. Fluids* **16**, 1719 (1973).
- ⁵⁵J. E. Kinsey, R. E. Waltz, and J. Candy, *Phys. Plasmas* **12**, 062302 (2005).
- ⁵⁶Y. Camenen, A. G. Peeters, C. Angioni, F. J. Casson, W. A. Hornsby, A. P. Snodin, and D. Strintzi, *Phys. Rev. Lett.* **102**, 125001 (2009).
- ⁵⁷Y. Camenen, A. G. Peeters, C. Angioni, F. J. Casson, W. A. Hornsby, A. P. Snodin, and D. Strintzi, *Phys. Plasmas* **16**, 062501 (2009).
- ⁵⁸N. Joiner, A. Hirose, and W. Dorland, *Phys. Plasmas* **17**, 072104 (2010).
- ⁵⁹Y. Ren, W. Guttenfelder, S. M. Kaye, E. Mazzucato, R. E. Bell, A. Diallo, C. W. Domier, B. P. LeBlanc, K. C. Lee, M. Podesta, D. R. Smith, and H. Yuh, *Nucl. Fusion* **53**, 083007 (2013).
- ⁶⁰R. L. Miller, M. S. Chu, J. M. Greene, Y. R. Lin-Liu, and R. E. Waltz, *Phys. Plasmas* **5**, 973 (1998).
- ⁶¹G. Rewoldt, W. M. Tang, S. Kaye, and J. Menard, *Phys. Plasmas* **3**, 1667 (1996).
- ⁶²R. R. Dominguez and G. M. Staebler, *Phys. Fluids B* **5**, 3876 (1993).
- ⁶³F. Casson, A. G. Peeters, Y. Camenen, W. A. Hornsby, A. P. Snodin, D. Strintzi, and G. Szepesi, *Phys. Plasmas* **16**, 092303 (2009).
- ⁶⁴R. Buchholz, S. Grosshauser, W. Guttenfelder, W. A. Hornsby, P. Migliano, A. G. Peeters, and D. Strintzi, *Phys. Plasmas* **22**, 082307 (2015).
- ⁶⁵Y. Camenen, Y. Idomura, S. Jolliet, and A. G. Peeters, *Nucl. Fusion* **51**, 073039 (2011).
- ⁶⁶R. E. Waltz, G. M. Staebler, and W. M. Solomon, *Phys. Plasmas* **18**, 042504 (2011).
- ⁶⁷Ö. D. Gurcan, P. H. Diamond, P. Hennequin, C. J. McDevitt, X. Garbet, and C. Bourdelle, *Phys. Plasmas* **17**, 112309 (2010).
- ⁶⁸F. I. Parra and P. J. Catto, *Plasma Phys. Controlled Fusion* **52**, 045004 (2010).
- ⁶⁹M. Barnes, F. I. Parra, J. P. Lee, E. A. Belli, M. F. F. Nave, and A. E. White, *Phys. Rev. Lett.* **111**, 055005 (2013).
- ⁷⁰J. C. Hillesheim, F. I. Parra, M. Barnes, N. A. Crocker, H. Meyer, W. A. Peebles, R. Scannell, A. Thornton, and the MAST Team, *Nucl. Fusion* **55**, 032003 (2015).